



Multifunctional polydopamine/hemin-cyclodextrin reinforced chitosan nanocomposite hydrogel: A synergistic platform for wound healing

Xu-Mei Zhang ^a, Man Zhang ^{b,c}, Ning-Ning Xu ^d, Shu-Juan Zheng ^{d,*}, Ni Cheng ^{c,**}

^a Department of Pathology, Affiliated Hospital of Weifang Medical University, Weifang, Shandong 261053, China

^b Department of Pharmacy, the First People's Hospital of Aksu Prefecture, Aksu, Xinjiang 843000, China

^c College of Pharmacy, Weifang Medical University, Weifang, Shandong 261053, China

^d Department of General Surgery, Affiliated Hospital of Weifang Medical University, Weifang, Shandong 261053, PR China



ARTICLE INFO

Keywords:

Chitosan
Dextran
Antibacterial hydrogel

ABSTRACT

Chronic cutaneous wounds present a significant challenge for healthcare providers globally, with the risk of bacterial infections emerging as a particularly concerning issue. There is an increasing need to employ a combination of diverse antibacterial strategies to address infections comprehensively in chronic wounds. This study introduces a highly efficient antibacterial platform that encapsulates the NO precursor (BNN6) into β -cyclodextrin-modified hemin-bearing polydopamine nanoparticles called NO/CHPDA. These nanoparticles are seamlessly integrated into a hydrogel composite comprised of L-arginine grafted chitosan (Arg-CS) and oxide dextran (oDex). The amalgamation of photothermal therapy (PTT), chemodynamic therapy (CDT), and nitric oxide (NO) antibacterial strategies within the NO/CHPDA@Arg-CS/oDex nanocomposite hydrogel demonstrates a synergistic and highly effective capacity to eradicate bacteria and accelerate the wound healing process *in vivo*. Remarkably, this nanocomposite hydrogel maintains excellent biocompatibility and induces minimal side effects. The resulting nanocomposite hydrogel represents a promising therapeutic solution for treating bacterial infections in wound healing applications.

1. Introduction

Chronic cutaneous wounds, a pervasive medical condition affecting a substantial proportion of the global population, continue to pose an ongoing challenge to healthcare providers worldwide [1,2]. These wounds are characterized by a persistent inability to heal, often resulting in significant morbidity and a reduced quality of life for affected individuals. The etiology of chronic wounds is complex and multifactorial, with numerous underlying factors such as aging, diabetes, and vascular disease contributing to their development and maintenance [2]. The prolonged non-healing nature of chronic wounds creates a favorable environment for bacterial colonization and proliferation, with subsequent infection often leading to further tissue damage and delayed healing [3,4]. Bacterial infections in wounds can result in many complications, including delayed healing, an increased risk of amputation, and even death. This is particularly concerning given the rising prevalence of antibiotic-resistant bacteria, which can complicate the

treatment of these infections [5].

Recently, there has been a growing interest in developing new and innovative approaches to treating wound bacterial infections [5–8]. Producing various antibacterial agents and strategies marks a significant milestone in this endeavor. These agents and strategies include chemotherapies utilizing diverse small molecules [9], quaternary ammonium polymers [10], and bactericidal metal ions such as Ag^{2+} , Zn^{2+} , and Cu^{2+} ions [11,12]. Additionally, novel approaches to sterilization, such as photothermal therapy (PTT) [13,14] or chemodynamic therapy (CDT) [15,16] have emerged. The PTT technique, a promising approach, involves using light-absorbing agents in the form of nanoparticles or dyes [13]. These agents generate heat upon exposure to near-infrared (NIR) light, leading to localized cell death.

In contrast, CDT employs a Fenton-type catalytic reaction to generate highly toxic hydroxyl radicals ($\cdot\text{OH}$), selectively damaging bacterial cells through oxidative stress [15]. While these antibacterial materials exhibit great potential, those relying on a single bactericidal model often

* Corresponding author at: Department of General Surgery, Affiliated Hospital of Weifang Medical University, 518# Fuyuan Street, Weifang 261053, Shandong, China.

** Corresponding author at: College of Pharmacy, Weifang Medical University, 7166# Baotong West Street, Weifang 261053, Shandong, PR China.

E-mail addresses: 1518391145@qq.com (S.-J. Zheng), chengnincn@163.com (N. Cheng).

struggle to achieve high efficiency, especially at low concentrations. Moreover, using such materials can lead to bacterial resistance during sterilization processes, posing a significant challenge in clinical settings. Consequently, there is an increasingly urgent demand for the advancement of antibacterial materials that employ diverse bactericidal approaches within the ongoing efforts of antibacterial research.

Nitric oxide (NO), a potential alternative to traditional antibiotics for infection treatment, has gained significant attention in recent years [17–19]. As a broad-spectrum antibacterial agent, NO can target a wide range of bacterial species. Its antibacterial properties stem from its ability to disrupt bacterial metabolism and DNA replication, ultimately leading to bacterial death. In contrast to traditional antibiotics that focus on specific components of bacterial cells, NO targets multiple pathways, rendering it more challenging for bacteria to develop resistance [18]. Beyond its antibacterial properties, NO also exhibits anti-inflammatory properties that may contribute to treating infectious diseases. By reducing inflammation, NO can help alleviate the damaging effects of the host's immune response to bacterial infections. Moreover, one particularly attractive function of NO is its ability to stimulate angiogenesis and promote the formation of new blood vessels in wound healing, which is crucial for delivering oxygen and nutrients to the wound site [20]. These characteristics make it a particularly appealing candidate for infection treatment. While NO offers advantageous properties for therapeutic applications, its practical utility is constrained by inherent challenges such as its gaseous nature and rapid release kinetics [21]. To address these obstacles, researchers have developed various NO-loading platforms, including liposomes, silica particles, dendrimers, hydrogel films, inverse opal scaffolds, and microneedle arrays, aiming to control NO delivery precisely [22]. While these platforms have yielded promising results, achieving controlled release and deeper NO diffusion remains challenging. Consequently, there is a pressing need to develop multifunctional platforms capable of providing controllable NO delivery for optimal wound healing outcomes.

Polysaccharide hydrogels show great promise for wound healing applications, owing to their remarkable biocompatibility, biodegradability, and the ability to establish a three-dimensional network that retains moisture and fosters tissue regeneration [23,24]. While chitosan has demonstrated desirable properties for the fabrication of polysaccharide hydrogels, such as mucoadhesion, hemostatic and anti-infective activity, low toxicity, and significant biodegradability, its rigid crystalline structure poses a considerable challenge to its practical utility in various applications due to its insolubility in aqueous medium. Consequently, extensive research efforts have been undertaken to explore the bioactive functionalization of chitosan, aiming to improve its solubility and enhance its functionality [25]. Recently, there has been a growing interest in using nontoxic and biocompatible amino acids to develop novel chitosan derivatives [26]. One amino acid that has garnered attention is L-arginine (L-Arg), a metabolically versatile agent crucial in numerous physiological processes. In addition to its role as an essential amino acid for protein synthesis, L-Arg has been found to stimulate the formation of blood vessels and promote tissue regeneration [27,28]. In a recent study conducted by Bratlie et al., it has been demonstrated that L-Arg possesses notable potential in augmenting collagen deposition, an indispensable constituent in the progression of cutaneous wound healing [29]. This discovery holds significant implications, given that collagen accumulation is central to restoring impaired tissue. Furthermore, the catabolism of L-Arg engenders pivotal nitrogenous compounds, mainly NO, which confers antibacterial attributes and assumes a critical function in collagen accumulation within nascent tissue [20]. These innovative revelations illuminate the multi-faceted advantageous effects of L-Arg in fostering the healing process and underscore its capacity as a therapeutic agent in managing wounds.

A highly efficient PTT/CDT/NO collaborative polysaccharide hydrogel antibacterial platform was engineered here. This platform was created by encapsulating the NO precursor *N,N'*-di-sec-butyl-*N,N'*-dinitroso-1,4-phenylenediamine (BNN6) into β -cyclodextrin (β -CD)-

modified hemin-bearing polydopamine nanoparticles (NO/CHPDA NPs), followed by incorporation into a hydrogel comprised of L-Arg grafted chitosan (Arg-CS)/oxide dextrans (oDex) (NO/CHPDA@Arg-CS/oDex). The designed nanocomposite hydrogel exhibits multifunctional properties for infected wound healing therapy. (1) The nanocomposite hydrogel demonstrates remarkable efficacy in PTT, generating a burst of heat upon near-infrared (NIR) light irradiation, leading to localized bacterial cell death. (2) Additionally, the nanocomposite hydrogel provides CDT to eliminate bacterial infections by continuously converting endogenous hydrogen peroxide into highly toxic hydroxyl radicals (\bullet OH), facilitated by the presence of hemin. (3) Notably, the nanocomposite hydrogel enables precise control over NO release, utilizing the heat generated from PTT. This has the benefit of removing bacteria, regulating inflammation, and stimulating angiogenesis. (4) The nanocomposite hydrogel displays excellent biocompatibility, water absorption, and permeability, creating a suitable microenvironment to mimic cell proliferation at wound sites. The amalgamation of PTT/CDT/NO antibacterial strategies within the NO/CHPDA@Arg-CS/oDex nanocomposite hydrogel has demonstrated a synergistic and efficacious ability to eliminate bacteria and expedite wound healing *in vivo*. It concurrently exhibits commendable biocompatibility and negligible side effects. The composite harbors immense potential as a therapeutic agent for bacteria-infected wound healing.

2. Experiment

2.1. Materials

Dopamine hydrochloride, L-Arginine, hemin and 3,3',5,5'-tetramethylbenzidine (TMB), 1-(3-(dimethylamino)propyl)-3-ethylcarbodiimide (EDC), N-hydroxysuccinimide (NHS), acetic acid (36 %), 1,4-Dithiothreitol (DTT) were acquired from Alfa Aesar. Tris(hydroxymethyl)methyl aminomethane (Tris) and sodium periodate (NaIO₄, 99.9 %) were purchased from Aladdin Biochemical Technology Co., Ltd. Dextran (MW ≈ 70 kDa) and chitosan (low molecular weight 120–150 kDa, deacetylation >75 %) were obtained from Shanghai Macklin Biochemical Co., Ltd. The mono-(6-mercaptop-6-deoxy)- β -cyclodextrin (β -CD-SH) was bought from Shandong BinzhouZhiyuan Biotechnology Co., Ltd. All the chemicals were used as received. Ultrapure water from Milli-Q Millipore Simplicity (Bedford, MA, USA) was used to prepare all solutions. All other chemical reagents utilized in this study were of analytical grade. The L929 cell line, procured from the American Type Culture Collection (ATCC) situated in Manassas, VA, USA, was utilized in this study. Additionally, standard strains of *Escherichia coli* (*E. coli*, catalog number ATCC 8739) and *Staphylococcus aureus* (*S. aureus*, catalog number ATCC 7755) were employed for the experimental investigations.

2.2. Synthesis of CHPDA nanoparticles

CHPDA nanoparticles were synthesized according to a previously reported method [30]. Initially, a solution was prepared by combining 6 mL of ethanol with 13.5 mL of deionized water and adding 200 μ L of 28 wt% ammonia solution while gently stirring at room temperature. After 30 min of continuous stirring, a solution containing hemin (50 mg hemin dissolved in 0.5 mL of DMF) and dopamine hydrochloride (75 mg dopamine hydrochloride dissolved in 0.5 mL of deionized water) was sequentially introduced into the mixture. The color of the solution changed from pale yellow to a rich dark brown throughout 24 h with continuous stirring. The noncovalent interactions, specifically π – π interactions, are established between the π bonds within the aromatic rings of hemin and polydopamine (PDA), facilitating the loading of hemin onto the PDA substrate. The resulting PDA/hemin (HPDA) nanoparticles were obtained through centrifugation and washed three times with water. To modify β -cyclodextrin (β -CD) on the surface of the HPDA nanoparticles, a 1 mL solution of HPDA (1 mg/mL) was first re-

dispersed into 4 mL of Tris-HCl buffer at pH 8.0. Subsequently, 5 µg of β-CD-SH and 2.5 mg of DTT were added to the solution, followed by an additional 24 h of stirring. Afterward, the CHPDA was subjected to three washes with water and re-dispersed into 5 mL of water for further applications.

For the BNN6-loading, 3 mg of CHPDA nanoparticles (1 mg/mL) were carefully mixed with 3 mL of BNN6 solutions (0.8 mg/mL in 30 % ethanol). The mixture was then stirred in brown vials for 24 h at room temperature. After incubation, the BNN6-loaded nanoparticles were separated from the solution through centrifugation at 12000 rpm for 15 min at 25 °C. Following incubation, the NO/CHPDA nanoparticles were separated from the solution by centrifugation. Subsequently, the obtained nanoparticles were washed three more times with water and subjected to lyophilization. The loading capacity of the nanoparticles was evaluated by measuring UV-visible absorption at 265 nm. The BNN6 loading efficiency was quantified using the following equation:

$$\text{Loading efficiency} = \frac{(C_{\text{BNN6 initially added}} - C_{\text{BNN6 remaining in the solution}}) \times V}{m} \times 100\%$$

2.3. Preparation of the hydrogel

The synthesis of L-Arg-grafted CS involved coupling L-Arg molecules to CS using a method previously described [31]. Conversely, the synthesis of oDex followed a described procedure [32]. Detailed procedures can be found in the supplementary material. The Arg-CS/oDex hydrogel was obtained through a dynamic crosslinking process between the amino groups (–NH₂) in the L-Arg-grafted CS and the aldehyde groups (–CHO) of oDex. Briefly, the Arg-CS polymer was dissolved in phosphate-buffered saline (PBS) with a pH of 7.4, resulting in a 0.5 wt% solution. Subsequently, CHPDA with 1, 2, and 4 wt% concentrations were dispersed in the Arg-CS solution using ultrasonication for approximately 20 min. Following this, oDex (dissolved in PBS to obtain a 20 wt% solution) was added to the above-prepared solution in a 1:1 volume ratio, leading to the immediate formation of the hydrogel.

2.4. Characterization

The nanoparticle size and zeta potential of CHPDA NPs were determined using the Zetasizer Nano ZS90 (Malvern, UK) under ambient conditions. To observe the morphologies of CHPDA NPs and the nanocomposite hydrogel, a transmission electron microscope (TEM) (OLYMPUS, veleta- 2kx2k, Japan) and scanning electron microscopy (SEM) (JSM-6510) were employed. The chemical composition of CHPDA and the nanocomposite hydrogel was investigated through SEM-EDS analysis and X-ray photoelectron spectra (XPS, Thermo Fisher, USA). Fourier transform infrared spectroscopy (FT-IR, VERTEX 70, Bremen, Germany) was employed to obtain infrared data, with small pieces of the samples mixed with KBr pellets. Support Information details the procedures for swelling ratio, *in vitro* degradability, rheological properties and porosity for the nanocomposite hydrogel.

2.5. Photothermal properties

The photothermal property was studied by monitoring the temperature increase within the near-infrared (NIR) laser irradiation on the CHPDA hydrogel solutions at varying concentrations. As a control, phosphate-buffered saline (PBS) temperature was also monitored under the same irradiation conditions. To further assess the photothermal stability, the CHPDA hydrogel solutions solution with a concentration of 200 µg/mL underwent five rounds of NIR laser irradiation, each round lasting for 1200 s and followed by a 1200 s interval.

2.6. NIR-stimulated NO release evaluation

The NIR-stimulated NO release from the NO/CHPDA hydrogel was investigated using a Griess reagent. The absorbance of the Griess reagent was initially measured in various concentrations of sodium nitrite (NaNO₂) to establish a standard curve. Subsequently, different NO/CHPDA hydrogel concentrations were irradiated with 808 nm light for different durations, followed by an incubation period with the Griess reagent. The resulting absorbance was quantified through UV – vis spectroscopy (Shimadzu, Japan).

2.7. Chemodynamic therapy activity evaluation

The oxidation of 3,3',5,5'- tetramethyl biphenyl (TMB) was conducted to investigate the peroxidase catalytic activity of the CHPDA nanocomposite hydrogel. A dispersion of the CHPDA nanocomposite hydrogel was initially prepared in acetate buffer (0.2 M, pH = 5.5, 2.0 mL). Subsequently, TMB (50 mM dissolved in DMSO, 10 µL) and H₂O₂ with various concentrations were added. The kinetics of this reaction were evaluated by closely monitoring the changes in absorbance at the wavelength of 652 nm using UV – vis spectroscopy (Shimadzu, Japan).

2.8. Antibacterial activity tests

The antibacterial efficacy of NO/CHPDA nanocomposite hydrogel was particularly focused on *Escherichia coli* (a Gram-negative bacterium) and *Staphylococcus aureus* (a Gram-positive bacterium), both widely recognized as representative strains. The sterility of the experimental apparatus is typically ensured by autoclaving before the experiments are conducted. Additionally, all samples undergo ultraviolet light irradiation for 30 min. The plate counting method was employed to determine the *in vitro* antibacterial efficiency of NO/CHPDA nanocomposite hydrogel with and without 808 nm NIR irradiation. Both *E. coli* and *S. aureus* bacterial liquid samples and the hydrogel samples were incubated at a temperature of 37 °C for 24 h. After incubation, the diluted bacterial solution was carefully placed on a culture dish previously coated with the solid medium. Subsequently, the bacterial colonies on the plates were meticulously photographed and counted, allowing for the calculation of the antibacterial rate.

2.9. Wound healing assay

The design of the skin wound animal experiment drew inspiration from established literature [33,34]. The animal experiments were conducted under the strict oversight and approval of the Animal Experimentation Committee at Weifang Medical University. Five-week-old BALB/c mice weighing between 14 g–18 g were obtained from Jinan Pengyue Experimental Animal Co., Ltd. These mice were acclimated in standard plastic rodent cages at a constant temperature for seven days before the start of the experiment. The dorsal area of each mouse was shaved and disinfected with 75 % alcohol to simulate wound infection. A circular wound, 6 mm in diameter, was made on the shaved area, and a suspension of *S. aureus* (1×10^6 CFU) was then applied to the wound. We conducted daily observations of the targeted wounds after applying different treatments, including PBS solution (control group), NIR (0.5 W/cm² irradiation for 10 min every other day), NO/CHPDA nanocomposite hydrogel (2 %, w/w), and nanocomposite hydrogel + NIR (0.5 W/cm² irradiation for 10 min every other day). Nanocomposite hydrogel injected into the irregular wound sites. On days 1, 7, and 14, photographs of the wounds were captured using a camera, and the wound areas were subsequently calculated using Image J software. Hydrogel was deliberately removed for better visibility during observation. On the 14th day, the wounds, as well as major organs (heart, liver, spleen, lungs, and kidneys), were excised and preserved in 4 % formaldehyde for subsequent histopathological analysis.

2.10. Cytotoxicity test and hemolysis assay

Mouse blood was collected from the eye and placed in a vessel with an anticoagulant. The blood sample was centrifuged at 5000 rpm for 10 min and then rinsed with PBS until the supernatant became clear. The erythrocytes (red blood cells) were combined with a solution containing NO/CHPDA nanocomposite hydrogel at varying concentrations and incubated at 37 °C for 4 h. After another round of centrifugation, the absorbance of the resulting supernatant was measured at 540 nm using a UV – vis spectroscopy instrument (Shimadzu, Japan).

For the cytotoxicity assessment, L929 fibroblast cells were cultivated in high-glucose Dulbecco's modified Eagle's medium within a humidified environment containing 5 % CO₂. All samples were subjected to sterilization via ultraviolet radiation for 2 h before the commencement of the experiment. The nanocomposite hydrogel and L929 fibroblast cells were introduced into a 96-well microplate and incubated at 37 °C for 24 h. The cytotoxicity of the nanocomposite hydrogel at different concentrations was assessed using the MTT method. Each experiment was replicated three times for reliability.

2.11. Statistical analysis

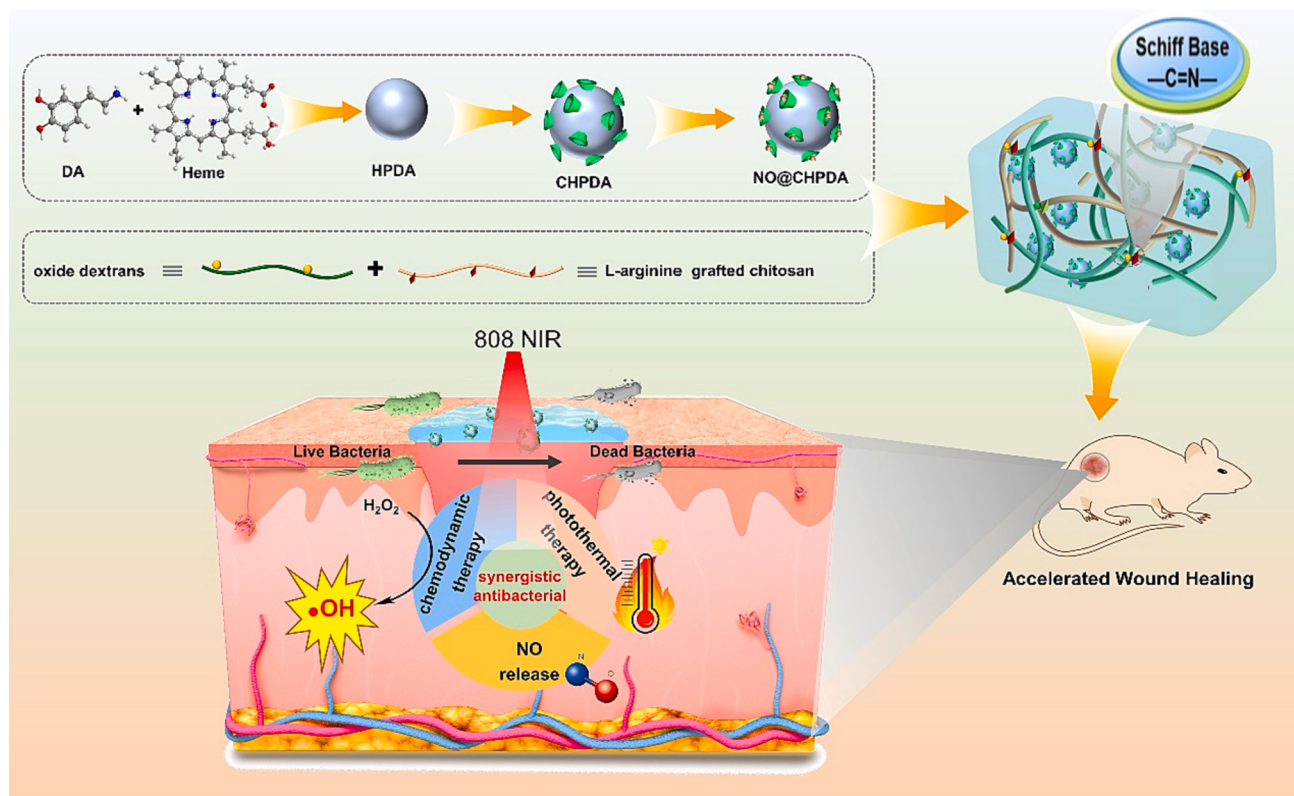
The experiments in this investigation were replicated three times, and the resulting data were presented as mean values with the corresponding standard deviations (\pm SD). The statistical significance between the two groups was evaluated using the widely accepted Student's *t*-test. *P* values below 0.05, 0.01, and 0.001 were deemed statistically significant for ease of interpretation and denoted with *, **, and ***, respectively. Conversely, *P*-values exceeding 0.05 were considered statistically non-significant (N.S.).

3. Results and discussion

3.1. Design and characterization of CHPDA nanoparticles

Here, the β -cyclodextrin (β -CD)-modified hemin-bearing polydopamine (PDA) nanoparticles (CHPDA) were prepared in two steps: (1) the hemin-bearing polydopamine(HPDA) was synthesized utilizing a facile one-pot method based on the self-polymerization of dopamine in alkaline solutions, and the hemin was doped in PDA via π - π stacking interactions [30]; (2) β -CD was grafted onto the PDA polymer through the nucleophilic addition reaction of the thiol nucleophilic group of 6-thio- β -CD (**Scheme 1**). In this nanoplatform, hemin (iron protoporphyrin) serves as the catalytic center of hemoglobin and exhibits excellent biological Fenton catalytic activity, thereby initiating CDT [35]. By grafting onto HPDA, β -CD possesses a hydrophobic cavity and hydrophilic outer faces, which endow the nanoparticles with NO delivery function [36]. Furthermore, the photothermal performance of PDA was employed to generate heat from absorbed NIR light, which facilitates desirable PTT antibacterial treatment, photothermal-enhanced CDT efficacy, and enables precise and on-demand NO release, achieving a PTT/CDT/NO collaborative antibacterial platform.

The size and morphology of CHPDA nanoparticles were assessed using transmission electron microscopy (TEM) and scanning electron microscopy (SEM). The surface of the CHPDA exhibited spheroidal aggregates with spatial distribution, as illustrated in Fig. 1a. The mean diameter of the nanoparticles was estimated to be approximately 100 nm. However, it should be noted that the presence of an β -CD layer was not detected through TEM due to its low density. To further investigate the size of the CHPDA nanoparticles, dynamic light scattering (DLS) was utilized. As depicted in Fig. 1b, the average hydration diameter was estimated to be 155 ± 11 nm, larger than the diameter observed through TEM, possibly due to the hydration effect. After grafting β -CD onto HPDA, the zeta potential decreased from -14.6 to -8.2 mV, indicating



Scheme 1. Schematic depiction of multifunctional polydopamine/hemin-cyclodextrin (CHPDA) reinforced Arg-CS/oDex nanocomposite hydrogel fabrication and its prospective utilization as a synergistic antibacterial platform for wound healing.

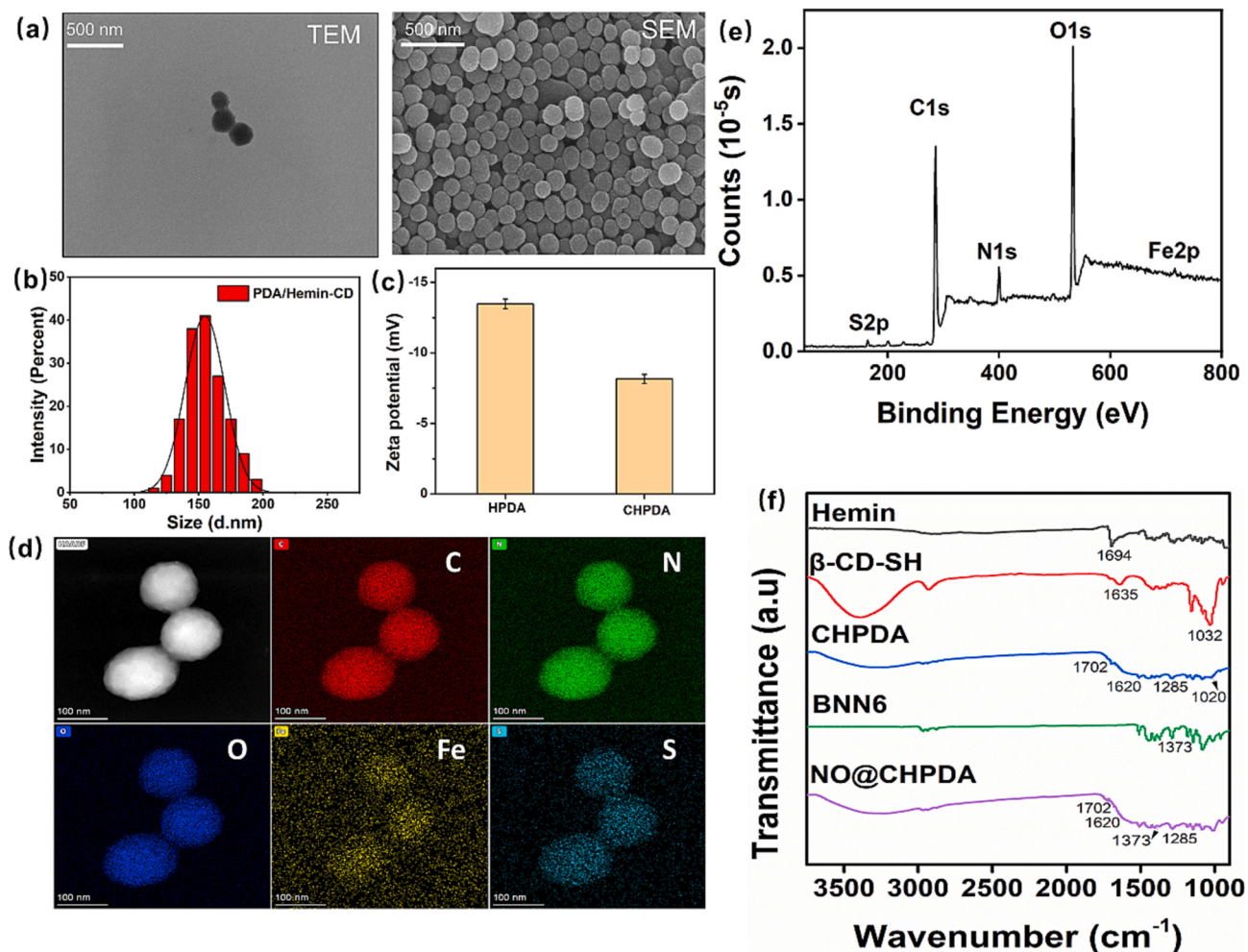


Fig. 1. Characterizations of CHPDA nanoparticles. (a) Representative TEM and SEM image of CHPDA nanoparticles. (b) Sizes and zeta potential (c) of CHPDA nanoparticles as investigated from DLS. (d) Elemental mappings of CHPDA nanoparticles. (e) XPS spectra of the CHPDA nanoparticles. (f) FT-IR spectra of hemin, β -CD-SH, CHPDA nanoparticles, BNN6, and NO@CHPDA nanoparticles.

the successful coating of β -CD on HPDA (Fig. 1c).

Furthermore, the elemental constitution of the CHPDA nanoparticles was analyzed using elemental mappings analysis (Fig. 1d). The results evidenced the existence of C, N, O, Fe, and S elements, as discerned from the spectra of CHPDA nanoparticles. The presence of Fe in the nanoparticles was ascertained to have originated from hemin, and the scant presence of S derived from 6-thiol- β -CD. X-ray photoelectron spectroscopy (XPS) was utilized to investigate the CHPDA nanosphere, as illustrated in Fig. 1e. The Fe2p peak, which appeared at approximately 711 eV, can be attributed to hemin [30]. Meanwhile, the peaks identified at approximately 163 and 227 eV were linked to S2p and S2s, respectively, originating from β -CD-SH [36]. These results are consistent with the mappings results, establishing the existence of hemin and β -CD molecules within the nanospheres.

Fourier transform infrared spectroscopy (FTIR) was employed to investigate the chemical composition and structural characteristics of the CHPDA nanoparticles (Fig. 1f). The peak observed at 1285 cm^{-1} in CHPDA corresponded to the stretching vibration of the phenolic (-OH) group on PDA. This observation is consistent with previous studies that have reported similar peaks for the phenolic groups in PDA [37]. Similarly, the peak located at 1694 cm^{-1} was assigned to the hemin's carboxylic group (-COOH) [30]. Interestingly, the peak at 1694 cm^{-1} shifted to 1702 cm^{-1} after CHPDA formed, indicating a strong interaction between PDA and hemin. This shift in the peak position may be attributed to the formation of hydrogen bonds between the hydroxyl

groups on PDA and the carboxylic group on hemin, which agrees with previous studies [36]. Furthermore, the peaks at 1635 and 1032 cm^{-1} , attributed to the -OH and C-O-C groups of β -CD-SH, respectively, shifted to 1620 and 1025 cm^{-1} after the formation of CHPDA [30]. Subsequently, the NO precursor BNN6 was loaded into the hydrophobic cavity structure of β -CD on the CHPDA nanoparticles [37]. The BNN6 loading efficiency was calculated to be 32.5 %, as determined by the standard curve using an ultraviolet spectrophotometer (Fig. S1). The UV-Visible spectra of CHPDA, NO@CHPDA, and BNN6, encompassing the absorption range from 200 to 800 nm, are elucidated in Fig. S2. Noteworthy is the emergence of an additional absorption peak around ~ 300 nm in both BNN6 and NO@CHPDA, an observation absent in the spectrum of CHPDA, thus affirming the loading of BNN6. The successful loading of BNN6 was further confirmed by FT-IR spectroscopy. The characteristic absorption peak of BNN6 at 1373 cm^{-1} , which corresponds to the deformation of N-N=O, was observed in the spectrum of NO@CHPDA (Fig. 1f). This finding provides further evidence of the successful loading of BNN6 into the hydrophobic cavity of β -CD through host-guest interaction.

3.2. Preparation and characterization of the CHPDA nanocomposite hydrogel

Applying polysaccharide wound dressings has demonstrated significant potential in promoting wound healing [23,24]. Oxidized dextran

was employed in conjunction with L-Arg grafted chitosan, with the reaction taking place through Schiff's base formation to fabricate a polysaccharide hydrogel. Dextrans, known for their clinical use in preventing vascular occlusion, have garnered attention in biomedical research due to their versatile and remarkable properties [32]. Among the various approaches to enhance the solubility and bioactivity of chitosan, the conjugation of L-Arg to CS has shown promise [26,31,38]. Additionally, to further improve the versatility of the hydrogel, NO/CHPDA was incorporated into the L-Arg grafted CS/oDex hydrogel. The nanocomposite hydrogels were fabricated through the amalgamation of NO/CHPDA NPs dispersed in Arg-CS aqueous medium and oDex in phosphate-buffered saline (PBS). This *in situ* gelation of the Arg-CS/oDex was primarily mediated by the formation of Schiff's base, arising from the interaction between the guanidine and amino groups of Arg-CS and the aldehyde moieties within oDex (Fig. 2a). Besides, the increase of NO/CHPDA concentration notably reduced the gelation time of the hydrogel, diminishing it from 60 s to 20 s, primarily ascribed to the heightened crosslinking density within the intricate nanocomposite hydrogel network (Fig. S3). Furthermore, the NO/CHPDA@Arg-CS/oDex nanocomposite hydrogel network underwent dynamic covalent crosslinking via Schiff's base, which could render the nanocomposite hydrogel with injectable capability. As illustrated in Fig. 2b, the nanocomposite hydrogel exhibited facile extrusion from a syringe without clogging. Hence, the nanocomposite hydrogels potential as an ideal candidate for wound dressing.

A porous microstructure is an essential criterion for a tissue-

engineered substitute as it facilitates crucial processes such as cell infiltration, nutrient, and oxygen diffusion, and removing cellular waste products from metabolism [39]. To gain insights into the porous architecture of hydrogel, SEM was used to capture detailed images, presented in Fig. 2c. The images revealed that the hydrogel exhibited a porous morphology along with rough surfaces that incorporated NO/CHPDA NPs. The roughness of the surface promotes enhanced cell attachment, thereby aiding in the regeneration of damaged tissue. This observation suggests that the microstructure of the hydrogel is of particular significance as it contributes to the acceleration of the wound-healing process. The investigation into the chemical compositions of Arg-CS/oDex nanocomposite hydrogel, supplemented with NO/CHPDA NPs, was meticulously carried out through the application of element mapping analysis. Notably, the distribution of the Fe component was detected, confirming the successful incorporation of NO/CHPDA NPs (Fig. 2d).

The FTIR spectra of pristine Arg-CS, oDex, blank Arg-CS/oDex hydrogel, and Arg-CS/oDex hydrogel loaded with various amounts of NO/CHPDA are depicted in Fig. 2e. The infrared spectrum of Arg-CS exhibits a distinctive tensile vibration band at the range of 1028–1062 cm⁻¹, corresponding to the C-O-C bond. This peak serves as a characteristic feature of CS [37]. Additionally, an absorption peak at 1552 cm⁻¹ is observed, representing the deformation vibration absorption of secondary amide (-N-H). The infrared absorption at approximately 1640 cm⁻¹ is observed, attributed to the stretching vibration of the carbonyl group (ν C=O) in the amide-I region. Moreover, a

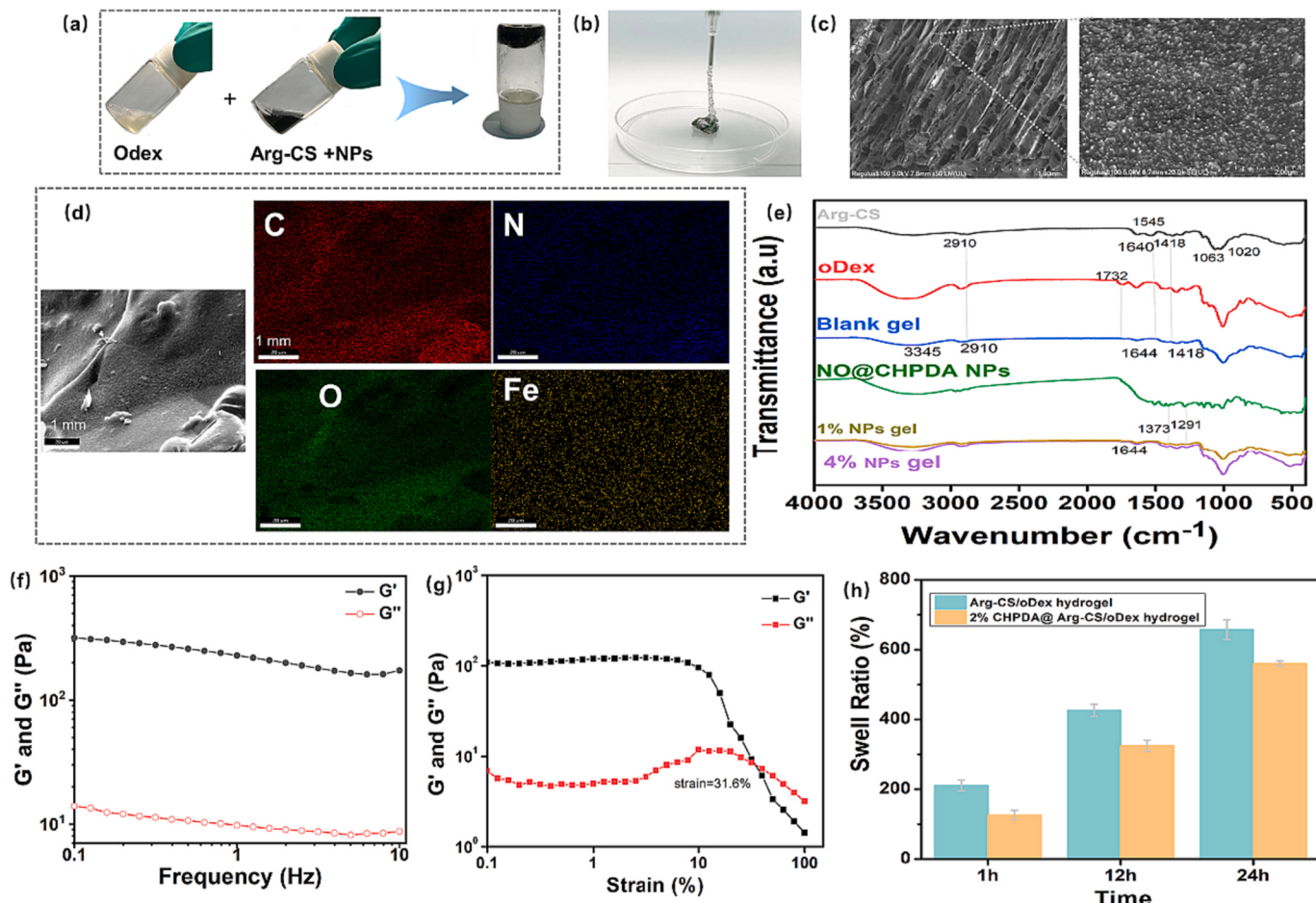


Fig. 2. Physical properties of CHPDA nanocomposite hydrogel. (a) Optical pictures of the sol-gel transition of Arg-CS/oDex nanocomposite hydrogel. (b) Photograph of the injectable hydrogel from a syringe. SEM (c) and (d) elemental mappings of NO/CHPDA @ Arg-CS/oDex hydrogel. (e) FT-IR spectra of Arg-CS, oDex, Arg-CS/oDex blank hydrogel, NO/CHPDA nanoparticles, Arg-CS/oDex hydrogel with different NO/CHPDA concentrations (1 and 4 wt%). (f) frequency dependence of the G' and G'' for the nanocomposite hydrogel. (g) G' and G'' of nanocomposite hydrogel on strain amplitude sweep. (h) Swelling properties of the nanocomposite hydrogel.

peak at 1418 cm^{-1} corresponding to the stretching vibration of the amide-III ($\nu\text{C-N}$) functionality is observed. This suggests the successful dehydration and condensation of the amino group ($-\text{NH}_2$) in CS and the carboxyl group ($-\text{COOH}$) in L-Arg, resulting in the formation of the acid amide bond [31]. This observation further confirms the successful grafting of L-Arg onto the CS backbone. The distinctive peak at 1732 cm^{-1} , corresponding to the stretching vibration of the aldehyde group in oDex, nearly disappears in the spectra of crosslinked Arg-CS/oDex hydrogel [32]. Simultaneously, a subdued absorbance peak at 1545 cm^{-1} , indicative of the primary amino group, is observed. Additionally, the hydrogel spectrum exhibits a band at 1644 cm^{-1} , attributed to $-\text{N}=\text{C}-$, affirming that the hydrogel has been formed through the reaction between amino groups and aldehyde groups [32]. Moreover, the characteristic bands of NO/CHPDA NPs experience amplification at 1373 and 1291 cm^{-1} with increasing concentration, providing substantial evidence for the successful loading of NPs into the Arg-CS/oDex nanocomposite hydrogel.

Furthermore, rheological examinations were conducted to probe the mechanical attributes of the NO/CHPDA@Arg-CS/oDex nanocomposite hydrogel. The storage modulus (G') and loss modulus (G'') values exhibited constancy at low strain variations, with G' surpassing G'' , affirming the gelation process. Frequency oscillation tests, depicted in Fig. 2f, underscore the stability of the adhesive within the 0.1 to 10 Hz range due to robust chemical cross-linking, specifically the Schiff's base. Evidently, the compressive stress-strain curves in Fig. 2g delineate a gel-sol transformation occurring when the strain exceeds 31.6% , indicating the nuanced mechanical behavior of the hydrogels. The tissue adhesive characteristics play a pivotal role in the pragmatic utilization for wound dressing. Investigation into the adhesive properties of composite hydrogels with diverse biological tissues, as illustrated in Fig. S4, reveals that tissues such as the heart, liver, spleen, lung, kidney, and muscle exhibit facile adherence to the $2.0\%-\text{NO}/\text{CHPDA@Arg-CS/oDex}$ nanocomposite hydrogel. This underscores the broad applicability of the nanocomposite hydrogel in adhering to various biological tissues, rendering it promising for diverse biomedical applications.

The assessment of the porosity of the NO/CHPDA NPs@Arg-CS/oDex nanocomposite hydrogel was conducted using the alcohol displacement method (Fig. S5). This method, involving the displacement of alcohol by the hydrogel material, provides valuable insights into the exchange of micronutrients and the capacity to absorb excess exudates at the wound site [40]. Notably, the NO/CHPDA nanocomposite hydrogel's porosity was marginally higher than that of the Arg-CS/oDex hydrogel. This disparity in porosity could be attributed to the diameter of the CHPDA microspheres, as illustrated in SEM images. Excessive wound effluence can impede the healing process by introducing surplus moisture to the wound environment. The exploration of water-absorption capabilities, as quantified by the swelling ratio of Arg-CS/oDex nanocomposite hydrogel. As depicted in Fig. 2h, the Arg-CS/oDex hydrogel manifested a remarkable maximum water absorption of approximately 600% of its initial weight after 24 h , indicating its viability as a wound dressing for efficiently absorbing tissue surplus exudates. Intriguingly, the incorporation of 2% CHPDA in the Arg-CS/oDex hydrogels resulted in a certain degree of decline in the equilibrium swelling ratio, registering at approximately 560% of their initial weight. This phenomenon is attributed to the gradual augmentation in the crosslinking density within the hydrogel matrix. Additionally, the *in vitro* degradation characteristics of the hydrogel were scrutinized within a PBS solution with a physiological pH of 7.4 , mirroring the normal physiological microenvironment. Over a 15 -day cultivation period, the hydrogel samples exhibited conspicuous weight reductions of approximately 70.2% , which could attribute to the cleavage of polysaccharide chains within the hydrogel (Fig. S6). Previous study reported that the hydrolytic degradability of CS-oDex hydrogels. [32] The degradation kinetics of CS-oDex hydrogels are intricately linked not only to the hydrolytic susceptibility of the Schiff's base but also to the concurrent degradation processes of CS and oDex. The results indicated the Arg-CS/oDex

nanocomposite hydrogel notable water-absorption and robust biodegradation capabilities, underscoring their potential utility as scaffolds in the field of tissue engineering.

3.3. Photothermal performance, NO release, and chemodynamic therapy activities of the CHPDA nanocomposite hydrogel

Considering the photothermal properties of PDA, the photothermal performances of CHPDA nanocomposite hydrogel were then evaluated. The CHPDA nanocomposite hydrogel exhibited concentration and power-dependent temperature increments when irradiated with an NIR laser, as depicted in Fig. 3a and b. Specifically, the 2% CHPDA nanocomposite hydrogel temperature reached $57.6\text{ }^\circ\text{C}$. In contrast, minimal temperature changes were observed in the blank hydrogel. These findings suggest that the CHPDA nanocomposite hydrogel possesses considerable photothermal conversion efficiency, enabling the nanocomposite hydrogel with NIR laser-induced photothermal therapy for wound healing. As illustrated in Fig. S7, the CHPDA nanocomposite hydrogel exhibited remarkable photothermal stability after undergoing five cycles, as evidenced by the sustained final temperature. The photothermal conversion efficiency analysis of CHPDA yielded a noteworthy efficiency of 38.6% , notably surpassing the efficiency observed for pure PDA at 18.4% , as depicted in Fig. S8. Similar photothermal enhancement achieved through the incorporation of hemin into PDA nanoparticles was reported by previous researchers [41]. These findings underscore the potential photothermal therapy using the CHPDA nanocomposite hydrogel.

The photothermal performance of NO/CHPDA nanocomposite hydrogel provided a convenient platform for constructing the NIR light-triggered NO-delivery systems, allowing for the precise and on-demand release of NO. As presented in Fig. 3c-d, the intelligent NO release characteristics were modulated by a binary "ON-OFF" NIR irradiation, indicating that NO release was stimulated by NIR irradiation, enabling the regulation of NO release. The NIR-triggered NO release system holds great promise for wound healing, where NO release can promote angiogenesis and enhance tissue regeneration. Incorporating NO/CHPDA nanoparticles into the nanocomposite hydrogel at a mass fraction between 1% and 4% resulted in a significant increase in NO released, ranging from approximately 1 to $4\text{ }\mu\text{M}$ (Fig. 3c).

As a protoporphyrin IX containing Fe^{3+} , hemin can provide an iron source to catalyze the conversion of H_2O_2 into toxic $\bullet\text{OH}$. We used $3,3',5,5'$ -tetramethyl biphenyl (TMB) as a substrate to evaluate the catalytic activities of the nanocomposite hydrogel [42]. In Fig. 3e, the blue oxTMB with a characteristic peak at 652 nm was observed, indicating that the CHPDA-based Fenton system produced the $\bullet\text{OH}$. The corresponding color change was also visually confirmed through photography (Fig. 3e, inset). The time-dependent absorbance variation of the solution was measured at 652 nm using a UV-Vis spectrophotometer (Fig. 3f). Results indicated that $\bullet\text{OH}$ generation occurred in a time- and H_2O_2 concentration-dependent manner. It is well-established that infected wounds usually exhibit an elevated degree of oxidative stress. The catalytic activities process effectively suppresses bacterial infections by converting H_2O_2 into toxic $\bullet\text{OH}$.

3.4. Antibacterial performance of the NO/CHPDA nanocomposite hydrogel

Considering the formidable photothermal effect, NO release, and catalytic activities of CHPDA nanocomposite hydrogel, we sought to investigate its anti-bactericidal properties against the gram-positive bacteria *S. aureus* and gram-negative bacteria *E. coli* using the agar plate counting method. As depicted in Fig. S9, it was observed that the anti-bactericidal activity of the nanocomposite hydrogel was concentration-dependent and influenced by NIR irradiation. Specifically, under NIR irradiation, a 7.5 mg/mL concentration of 2% CHPDA nanocomposite hydrogel resulted in a killing rate of approximately 98%

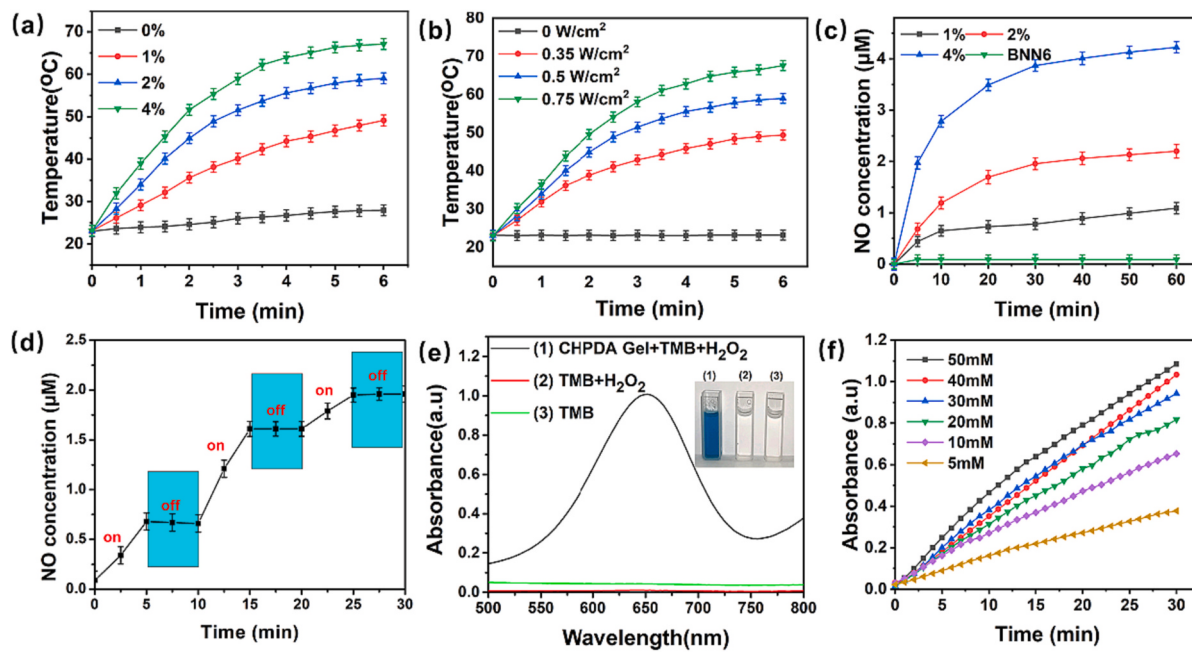


Fig. 3. Versatile activities of CHPDA nanocomposite hydrogel. Photothermal effect of CHPDA nanocomposite hydrogel (a) at different concentrations (wt%) upon irradiation (808 nm, 0.5 W/cm², 6 min) and (b) at different NIR power densities (2.5 mg/mL of 2 wt% nanocomposite hydrogels, 6 min). (c) NO release profiles of different concentrations (wt%) of nanocomposite hydrogel (10 mg/mL) after 808 nm NIR irradiated at 0.5 W/cm². (d) NIR controllability release performance of 2 wt % nanocomposite hydrogel (10 mg/mL) at 0.5 W/cm². (e) UV-visible absorption spectra and accompanying visual alterations (inset) during the catalytic oxidation of TMB (oxTMB) within the reaction buffer at pH 5.5. (f) Time-dependent changes in absorbance at 652 nm result from the catalytic oxidation of TMB at varying concentrations of H₂O₂.

for both bacteria. In contrast, without NIR irradiation, the killing rate was only 66.8 % at the same concentration. These results indicate that CHPDA nanocomposite hydrogel possesses significant antibacterial properties against gram-negative and gram-positive bacteria, with NIR

irradiation enhancing the anti-bactericidal effectiveness.

To further investigate the synergistic antibacterial efficacy, bacteria were treated differently with and without NIR irradiation as follows: (1) control; (2) blank hydrogel; (3) BNN6@ hydrogel; (4) H₂O₂; (5) CHPDA

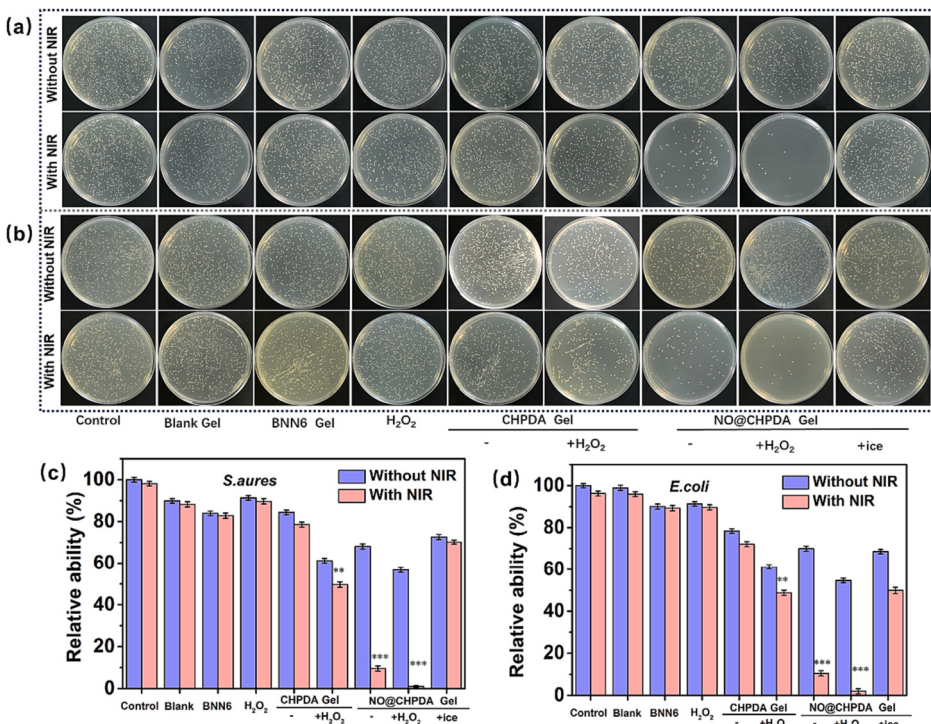


Fig. 4. Assessment of antibacterial efficacy in CHPDA nanocomposite hydrogel. Microbial colony visualization of *S. aureus* (a) and *E. coli* (b) following treatment with varying formulations of nanocomposite hydrogel with or without 808 nm laser irradiation (0.5 W/cm², 10 min). The plate count method measured the quantitative bacterial viabilities of *S. aureus* (c) and *E. coli* (d).

nanocomposite hydrogel (6) CHPDA nanocomposite hydrogel + H₂O₂; (7) NO/CHPDA nanocomposite hydrogel; (8) NO/CHPDA nanocomposite hydrogel + H₂O₂; (9) NO/CHPDA nanocomposite hydrogel + ice. As displayed in Fig. 4, the blank hydrogel, BNN6 hydrogel, H₂O₂, and CHPDA nanocomposite hydrogel alone exhibited minimal antibacterial activity, as demonstrated by the slight reduction in colony numbers compared to the control group, regardless of NIR irradiation. Moreover, the number of colonies was reduced in the CHPDA nanocomposite hydrogel + H₂O₂ group due to the generation of •OH via Fenton-like catalysis of H₂O₂. These observations suggest that a single PTT, NO-release, or catalytic treatment holds limited weak antibacterial efficacy. Notably, synergistic PTT, NO, and catalytic therapy were achieved by combining NO/CHPDA nanocomposite hydrogel + H₂O₂+NIR, resulting in a nearly 90 % decrease in bacterial colonies. In the absence of NO or NIR irradiation or the presence of ice, the antibacterial effect of NO/CHPDA nanocomposite hydrogel is considerably diminished. This finding provides compelling evidence for the synergistic antibacterial efficacy derived from the combined therapy.

To further explore the antibacterial mechanism of CHPDA + NIR, we employed TEM to scrutinize alterations in the morphologies of *E. coli* and *S. aureus*. As depicted in the TEM images in Fig. S10, the rod-shaped morphology of *E. coli* in the control group, with a smooth cell wall, signified a healthy bacterial state. Intriguingly, notable changes in bacterial morphology transpired in the CHPDA group upon exposure to NIR. The cell membrane of the CHPDA + NIR group was severely disrupted, leading to content leakage, providing unequivocal evidence of the potent bactericidal efficacy of this synergistic system. Analogously, for *S. aureus*, morphological transformations mirrored those observed for *E. coli*, substantiating the conclusion that CHPDA + NIR achieves bacterial elimination through the deleterious disruption of bacterial cell membranes. The NO/CHPDA nanocomposite hydrogel's antibacterial potential was evaluated by applying a live/dead kit in conjunction with fluorescent microscopy (Fig. 5). These analyses corroborated the findings obtained from the colony formation counting assays, revealing the limited efficacy of individual PTT, CDT, or NO release treatments in suppressing bacterial growth. However, when the bacteria were exposed to NIR irradiation and H₂O₂ in the presence of the NO/CHPDA nanocomposite hydrogel, conspicuous red fluorescence was observed, indicating a vast scale of dead bacterial cells. This observation provides

compelling evidence of the synergistic antibacterial efficacy of the nanocomposite hydrogel attributed to the combined effects of PTT, NO, and catalytic therapy. Upon exposure to NIR irradiation, the nanocomposite hydrogel undergoes a rapid rise in temperature, generating heat that can disrupt the bacterial membrane. Subsequently, the generated heat triggered NO release, which may furnish a promising avenue for mitigating bacterial activity accomplished via lipid peroxidation and DNA deamination of bacterial cells. Additionally, catalytic therapy can efficiently activate the transformation of a lower dose of H₂O₂ into •OH, leading to oxidative damage and, ultimately, bacterial death. Thus, it can be concluded that the NO@CHPDA nanocomposite hydrogel holds great promise as a potent antibacterial application.

3.5. *In vivo* wound healing experiment

Enlightened by the potential of the proposed multifunctional platform, which exhibits both remarkable antimicrobial properties and excellent biocompatibility, our study focuses on the application prospects of the NO/CHPDA nanocomposite hydrogel in the disinfection and healing of animal wounds. To assess the antibacterial effect and wound healing properties of the CHPDA nanocomposite hydrogel under laser irradiation, we conducted experiments on a mouse model with full-thickness skin defects infected by *S. aureus* (Fig. 6a). The experimental treatments were categorized into four distinct groups: the CHPDA nanocomposite hydrogel with laser irradiation (0.5 W/cm² irradiation for 10 min every other day), the CHPDA nanocomposite hydrogel without laser irradiation, laser irradiation (0.5 W/cm² irradiation for 10 min every other day) denoted as NIR, and PBS treatment (control).

We recorded the real-time temperature using a thermal imaging camera to monitor the effects of NIR phototherapy on the wounds treated with the CHPDA nanocomposite hydrogel *in vivo*. As demonstrated in Fig. 6b, the temperature of the tumor tissues in the NO/CHPDA nanocomposite hydrogel group rapidly increased to 50.9 °C, which is adequately high to eliminate the surrounding bacteria, thereby promoting wound healing effectively. In contrast, the temperature only slightly changed with PBS treatment in the control group, indicating the remarkable PTT property of the NO/CHPDA nanocomposite hydrogel. This observation aligned with the findings of our *in vitro* photothermal test. During wound healing, it was observed that applying NIR light did

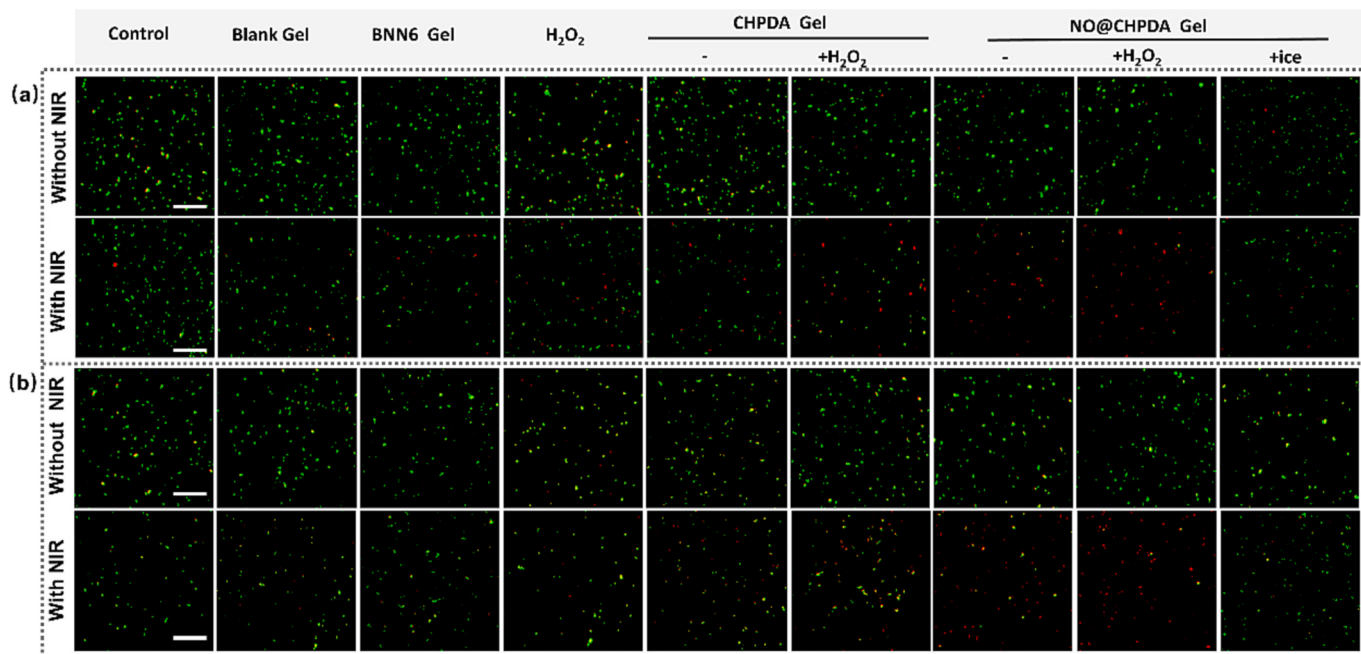


Fig. 5. Fluorescence images capturing *S. aureus* (a) and *E. coli* (b) bacteria subjected to various treatments with DMAO and EthD-III double staining.

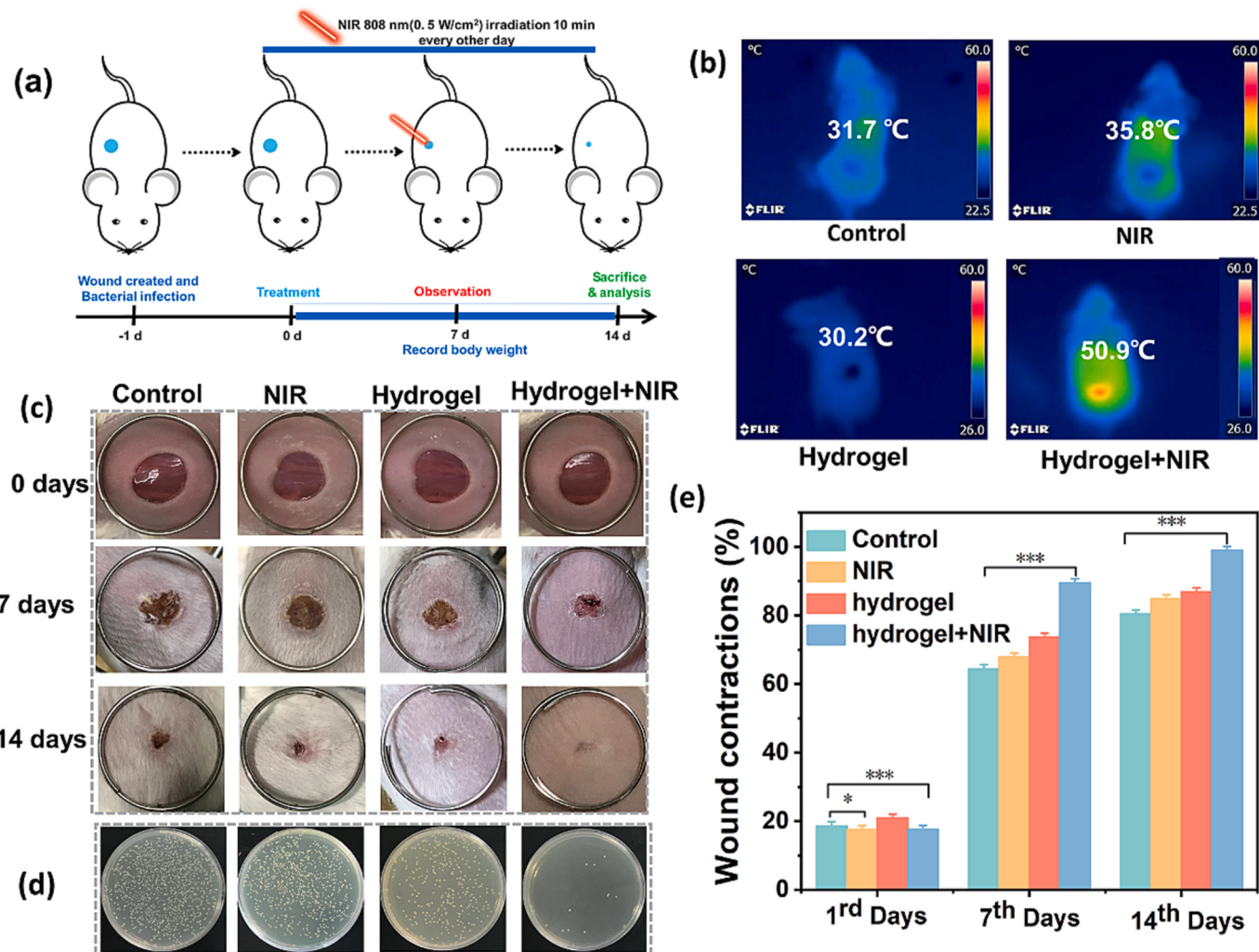


Fig. 6. Experimental design and healing progress in *S. aureus*-infected wounds. (a) Schematic representation of the animal experiment. (b) Infrared thermographic images capture mice's thermal response subjected to laser irradiation at an intensity of 0.5 W/cm^2 for 10 min. Graphical representation (c) and quantitative data (e) of the assessment of wound area on days 7 and 14. (d) A collection of photographs concerning the bacterial colonies inhabiting infected wounds on day 7.

not result in any discernible dermal injury at the irradiation site.

Meanwhile, the wound healing process was assessed by capturing images of the wound sites on days 1, 7, and 14 using a digital camera (Fig. 6c). Notably, the group treated with the NO/CHPDA nanocomposite hydrogel combined with NIR irradiation exhibited the most rapid healing and least scarring compared to the other treatment groups. These findings provide compelling evidence for the superior wound healing efficacy of NO/CHPDA hydrogel with NIR irradiation. After a 14-day treatment period, the wounds in the NO/CHPDA nanocomposite hydrogel + NIR groups approached near-complete healing. In contrast, the wounds in the control, NIR, and NO/CHPDA nanocomposite hydrogel groups showed limited progress. To further quantify the extent of wound healing, Fig. 6e presents the quantization results. Following a 7-day treatment period, applying NO/CHPDA nanocomposite hydrogel in combination with near-infrared (NIR) yielded a healing rate of 89.5 %. Conversely, solely utilizing the nanocomposite hydrogel resulted in a healing rate of 73.6 %. In contrast to the control group, the sole application of NIR treatment exhibited a enhanced efficacy in fostering wound healing. This phenomenon may be attributed to local temperature increases induced by NIR, as studies indicate that controlled elevation of temperature within a certain range can promote wound healing [43,44]. Astonishingly, on the 14th day, the group treated with the nanocomposite hydrogel in conjunction with NIR exhibited a remarkable reduction in wound size, reaching nearly 100 %, surpassing

the reductions observed in control (80.4 %), NIR (84.8 %), and hydrogel composites (86.8 %) groups. The superior bactericidal effectiveness of NIR-irradiated CHPDA nanocomposite hydrogel was corroborated through *in vivo* antibacterial assessments (Fig. 6d), aligning with the findings from *in vitro* antibacterial evaluations.

To verify the progress of wound healing under different treatments, we examined histological images with hematoxylin and eosin (H&E) staining of wound tissue obtained on day 14. As presented in Fig. 7, analysis of the collected images verified the wound-healing process. In the control and NIR groups, evident infiltration of inflammatory cells was observed in the skin sections, indicating the acute inflammatory response occurring in the wound. Conversely, administering NO/CHPDA nanocomposite hydrogel alone was found to stimulate the production of dermal tissue and the regeneration of resilient collagen fibers, thereby demonstrating the efficacy of NO/CHPDA hydrogel in promoting wound healing. Remarkably, in the CHPDA nanocomposite hydrogel + NIR treatment group, a clear and intact epidermal-dermal connection was observed in the histological images stained with H&E, thus providing further evidence to substantiate the synergistic effect of the Fenton reaction and PTT in facilitating a superior wound healing outcome.

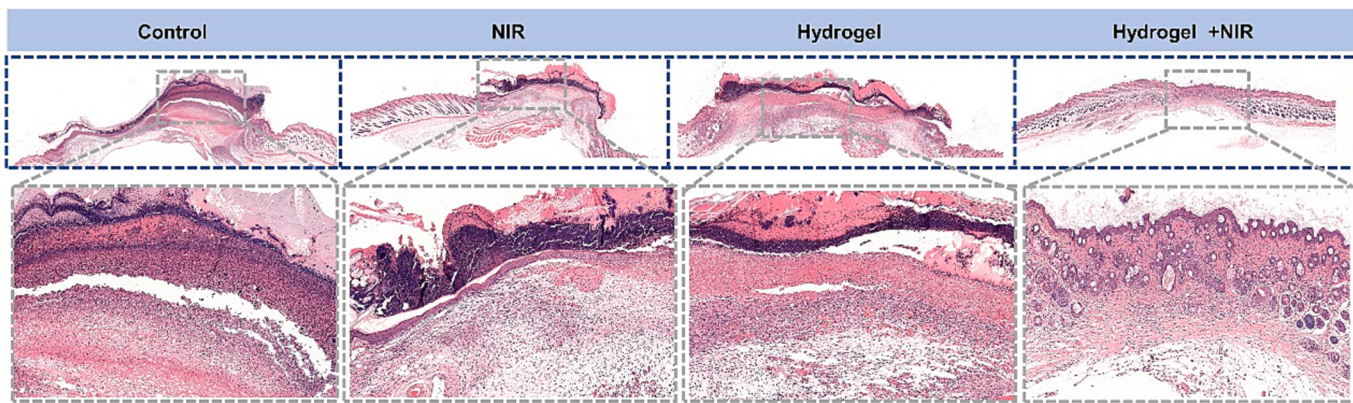


Fig. 7. Histomorphological examination of wound regeneration. H&E staining of wounds subjected to different treatments on day 14.

3.6. In vitro bioactivity and biocompatibility

Favorable bioactivity and biocompatibility are essential properties of materials used in wound healing applications. The live/dead staining assay with Calcein-AM/PI was conducted to assess cytocompatibility further. As presented in Fig. 8a, almost all the L929 cells were stained green, indicating their viability, and no dead cells (red fluorescence) were observed. Further, the cytocompatibility of NO/CHPDA nanocomposite hydrogel was measured using MTT assay by directly contacting mouse-derived fibroblast (L929) cells. The results, depicted in Fig. 8b, demonstrated an increasing trend with concentration, indicating that the composite hydrogel did not exhibit significant toxicity and even stimulated cell proliferation. This phenomenon is likely ascribed to NIR stimulation inducing the release of NO from nanocomposite hydrogels, a correlation validated by previous study [45]. This process is believed to positively impact the growth of endothelial cells, fibroblasts, and keratinocytes, thereby promoting the overall healing process. Upon NIR irradiation, the nanocomposites elicited a measure of toxicity, notably at a higher concentration (8 mg/mL), a phenomenon likely attributed to the heightened release of NO and concurrent uncontrolled temperature escalation. Nevertheless, the cell viabilities post-incubation remained consistently above 85 %, even at the elevated concentration of 8 mg/mL, underscoring the inherent low toxicity of the nanocomposites toward human normal cells.

Wound dressings play a crucial role in the healing process of injured tissue, as they are in direct contact with blood and other biological components. Therefore, wound dressings must possess hemocompatibility, as it ensures the safety and efficacy of the wound dressing. To evaluate the hemocompatibility of the NO/CHPDA nanocomposite hydrogel, hemolysis tests were conducted (Fig. 8c). The nanocomposite hydrogel was found to have a hemolysis rate of <1.5 % even at high concentrations of 2 mg/mL, which is comparable to the negative control (PBS) and meets the standard set by the American Society for Testing and Materials (ASTM F 756-00). During our investigation, we comprehensively assessed the mice's body weight throughout the entire treatment regimen. Fig. S11 shows that none of the treatment groups exhibited any statistically significant alterations in body weight. To ascertain the safety profile of the interventions under scrutiny, we pursued a critical evaluation through pathological examination of vital organs, including the heart, liver, spleen, lung, and kidney. Subsequently, we meticulously examined these major organs by employing H&E staining techniques for histological analysis (Fig. 8d). Our examination yielded no discernible evidence of toxicity or adverse effects in any examined organs. The excellent compatibility and necessary hemocompatibility exhibited by the hydrogel suggested its great potential for tissue engineering applications.

Addressing bacterial infections, a pervasive challenge in wound healing, necessitates innovative strategies [1,2]. In this study, the

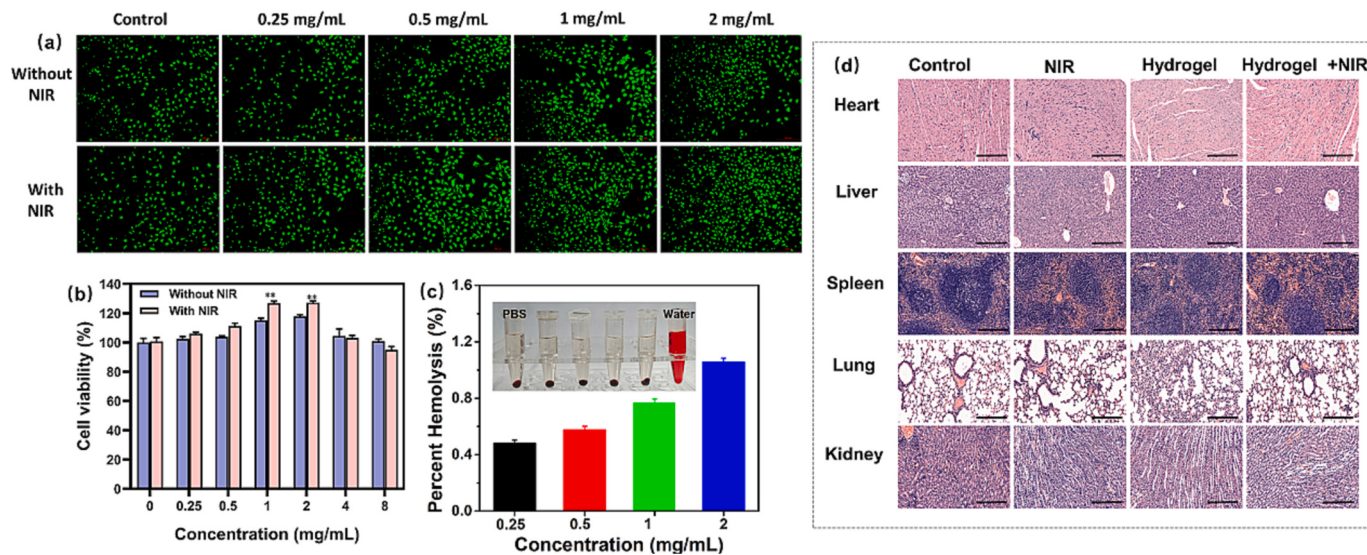


Fig. 8. Evaluation of biocompatibility for CHPDA nanocomposite hydrogel. Live/Dead cell staining (a) and viability (b), elucidating the cellular response to the CHPDA hydrogel across different concentrations. (c) Hemolytic effects induced by the CHPDA nanocomposite hydrogel at varying concentrations. (d) Histological investigations of major organs with the H&E staining in mice after treatment.

integration of PTT, CDT, and NO within the NO/CHPDA@Arg-CS/oDex nanocomposite hydrogel has showcased a synergistic and potent antibacterial capability, fostering accelerated wound healing. The inclusion of CHPDA nanoparticles bestowed the composite hydrogel with heightened antibacterial efficacy, capitalizing on the synergistic effects of multiple therapeutic modalities. While prior research employed metal-based nanoparticles like silver nanoparticles [46], copper nanoparticles [47], gold nanoparticles [48], and zinc nanoparticles [49] in hydrogels for synergistic antibacterial activity, their widespread use is impeded by nonspecific biological toxicity and potential long-term retention *in vivo*. In contrast, naturally derived β -CD-modified hemin-bearing polydopamine offers enhanced biocompatibility. Moreover, the introduction of Arg-CS into the composite hydrogel remarkably augmented angiogenesis, tissue regeneration, and collagen accumulation. These outcomes underscore the multifaceted benefits of the NO/CHPDA nanocomposite hydrogel, enhancing swelling capacity, biocompatibility, water absorption, and permeability, thereby creating a conducive microenvironment mimicking cell proliferation at wound sites. However, a notable limitation lies in the hydrogel's relatively low mechanical strength in its swollen state, necessitating improvements to match the resilience of hard tissues. Additionally, an excessive concentration of hydrogels, potentially leading to uncontrolled temperature increases, poses a risk of thermal damage to surrounding healthy tissue. These considerations underscore the ongoing need for refinement in achieving optimal skin repair, signifying that there is still a substantial journey ahead.

4. Conclusion

In summary, we present a synergistic antibacterial polysaccharide nanocomposite hydrogel integrated PTT/CDT/NO antibacterial strategies for bacteria-infected wound healing therapy. The fabrication of this nanocomposite hydrogel entails encapsulating the NO precursor, BNN6, within the β -CD modified hemin-bearing PDA (NO/CHPDA). Subsequently, the NPs are seamlessly incorporated into a hydrogel matrix composed of L-Arginine grafted chitosan and oxide dextrans. The NO/CHPDA endows the nanocomposite hydrogel with PTT, CDT, and NO release activity, providing a synergistic platform for bacteria-infected wounds. The integration of PTT/CDT/NO antibacterial strategies within the NO/CHPDA@Arg-CS/oDex nanocomposite hydrogel has demonstrated a synergistic and efficacious ability to eliminate bacteria and expedite wound healing *in vivo* while concurrently exhibiting commendable biocompatibility and negligible side effects. This nanocomposite hydrogel material possesses immense potential as a therapeutic agent for treating bacteria-infected wounds.

CRediT authorship contribution statement

Xu-Mei Zhang: Conceptualization, Data curation, Investigation, Methodology, Resources, Writing – original draft. **Man Zhang:** Data curation, Investigation, Methodology, Visualization. **Ning-Ning Xu:** Investigation, Methodology, Visualization. **Shu-Juan Zheng:** Methodology, Resources, Supervision, Writing – review & editing. **Ni Cheng:** Conceptualization, Funding acquisition, Methodology, Project administration, Resources, Writing – original draft, Writing – review & editing.

Declaration of competing interest

The authors declare that they have no known competing financial interests or personal relationships that could have appeared to influence the work reported in this paper.

Data availability

Data will be made available on request.

Acknowledgements

The authors are grateful for the generous financial support from the National Natural Science Foundation of China (Grant No. 21901186), Weifang Science and Technology Development Program Projects (Grant No. 2021YX032), and Development Plan for Youth Innovation Team in Higher School of Shandong Province (2022KJ265). We thank Home for Researchers editorial team (www.home-for-researchers.com) for language editing service.

Appendix A. Supplementary data

Supplementary data to this article can be found online at <https://doi.org/10.1016/j.ijbiomac.2024.129553>.

References

- [1] M. Xue, R. Zhao, H. Lin, C. Jackson, Delivery systems of current biologicals for the treatment of chronic cutaneous wounds and severe burns, *Adv. Drug Deliv. Rev.* 129 (2018) 219–241, <https://doi.org/10.1016/j.addr.2018.03.002>.
- [2] E. Darwin, M. Tomic-Canic, Healing chronic wounds: current challenges and potential solutions, *Curr. Derm. Rep.* 7 (4) (2018) 296–302, <https://doi.org/10.1007/s13671-018-0239-4>.
- [3] S.A. Eming, P. Martin, M. Tomic-Canic, Wound repair and regeneration: mechanisms, signaling, and translation, *Sci. Transl. Med.* 6 (265) (2014), <https://doi.org/10.1126/scitranslmed.3009337>, 265sr6–265sr6.
- [4] A.R. Siddiqui, J.M. Bernstein, Chronic wound infection: facts and controversies, *Clin. Dermatol.* 28 (5) (2010) 519–526, <https://doi.org/10.1016/j.cldermatol.2010.03.009>.
- [5] F. Zhao, Y. Su, J. Wang, S. Romanova, D.J. DiMaio, J. Xie, S. Zhao, A highly efficacious electrical biofilm treatment system for combating chronic wound bacterial infections, *Adv. Mater.* 35 (6) (2023) 2208069, <https://doi.org/10.1002/adma.202208069>.
- [6] S. Das, A.B. Baker, Biomaterials and Nanotherapeutics for enhancing skin wound healing, *Front. Bioeng. Biotechnol.* 4 (2016), <https://doi.org/10.3389/fbioe.2016.00082>.
- [7] H.S. Kim, X. Sun, J.-H. Lee, H.-W. Kim, X. Fu, K.W. Leong, Advanced drug delivery systems and artificial skin grafts for skin wound healing, *Adv. Drug Deliv. Rev.* 146 (2019) 209–239, <https://doi.org/10.1016/j.addr.2018.12.014>.
- [8] M. Morey, A. Pandit, Responsive triggering systems for delivery in chronic wound healing, *Adv. Drug Deliv. Rev.* 129 (2018) 169–193, <https://doi.org/10.1016/j.addr.2018.02.008>.
- [9] M. Zhou, M. Zheng, J. Cai, Small molecules with membrane-active antibacterial activity, *ACS Appl. Mater. Interfaces* 12 (19) (2020) 21292–21299, <https://doi.org/10.1021/acsami.9b20161>.
- [10] Y. Jiao, L.-N. Niu, S. Ma, J. Li, F.R. Tay, J.-H. Chen, Quaternary ammonium-based biomedical materials: state-of-the-art, toxicological aspects and antimicrobial resistance, *Prog. Polym. Sci.* 71 (2017) 53–90, <https://doi.org/10.1016/j.progpolymsci.2017.03.001>.
- [11] M. Godoy-Gallardo, U. Eckhard, L.M. Delgado, Y.J.D. de Roo Puente, M. Hoyos-Nogués, F.J. Gil, R.A. Perez, Antibacterial approaches in tissue engineering using metal ions and nanoparticles: from mechanisms to applications, *Bioact. Mater.* 6 (12) (2021) 4470–4490, <https://doi.org/10.1016/j.bioactmat.2021.04.033>.
- [12] R. Pachaiappan, S. Rajendran, P.L. Show, K. Manavalan, M. Naushad, Metal/metal oxide nanocomposites for bactericidal effect: a review, *Chemosphere* 272 (2021) 128607, <https://doi.org/10.1016/j.chemosphere.2020.128607>.
- [13] Y. Chen, Y. Gao, Y. Chen, L. Liu, A. Mo, Q. Peng, Nanomaterials-based photothermal therapy and its potentials in antibacterial treatment, *J. Control. Release* 328 (2020) 251–262, <https://doi.org/10.1016/j.jconrel.2020.08.055>.
- [14] Y. Zou, Y. Zhang, Q. Yu, H. Chen, Photothermal bactericidal surfaces: killing bacteria using light instead of biocides, *Biomater. Sci.* 9 (1) (2021) 10–22, <https://doi.org/10.1039/DOBM00617C>.
- [15] C. Jia, Y. Guo, F.-G. Wu, Chemodynamic therapy via Fenton and Fenton-like nanomaterials: strategies and recent advances, *Small* 18 (6) (2022) 2103868, <https://doi.org/10.1002/smll.202103868>.
- [16] J. Qi, G. Jiang, Y. Wan, J. Liu, F. Pi, Nanomaterials-modulated Fenton reactions: strategies, chemodynamic therapy and future trends, *Chem. Eng. J.* 466 (2023) 142960, <https://doi.org/10.1016/j.cej.2023.142960>.
- [17] L. Yang, E.S. Feura, M.J.R. Ahonen, M.H. Schoenfisch, Nitric oxide-releasing macromolecular scaffolds for antibacterial applications, *Adv. Healthc. Mater.* 7 (13) (2018) 1800155, <https://doi.org/10.1002/adhm.201800155>.
- [18] W. Wang, H. Sheng, D. Cao, F. Zhang, W. Zhang, F. Yan, D. Ding, N. Cheng, S-nitrosoglutathione functionalized polydopamine nanoparticles incorporated into chitosan/gelatin hydrogel films with NIR-controlled photothermal/NO-releasing therapy for enhanced wound healing, *Int. J. Biol. Macromol.* 200 (2022) 77–86, <https://doi.org/10.1016/j.ijbiomac.2021.12.125>.
- [19] J.R. Hall, K.R. Rouillard, D.J. Suchta, M.D. Brown, M.J.R. Ahonen, M.H. Schoenfisch, Mode of nitric oxide delivery affects antibacterial action, *ACS Biomater. Sci. Eng.* 6 (1) (2020) 433–441, <https://doi.org/10.1021/acsbiomaterials.9b01384>.

- [20] H. Meurs, S. McKay, H. Maarsingh, M.A.M. Hamer, L. Macic, N. Molendijk, J. Zaagsma, Increased arginase activity underlies allergen-induced deficiency of cNOS-derived nitric oxide and airway hyperresponsiveness, *Br. J. Pharmacol.* 136 (3) (2002) 391–398, <https://doi.org/10.1038/sj.bjp.0704725>.
- [21] Y. Duan, Y. Wang, X. Li, G. Zhang, G. Zhang, J. Hu, Light-triggered nitric oxide (NO) release from photoresponsive polymersomes for corneal wound healing, *Chem. Sci.* 11 (1) (2020) 186–194, <https://doi.org/10.1039/C9SC04039K>.
- [22] A. Jones, J. Pant, E. Lee, M.J. Goudie, A. Gruzd, J. Mansfield, A. Mandal, S. Sharma, H. Handa, Nitric oxide-releasing antibacterial albumin plastic for biomedical applications, *J. Biomed. Mater. Res. Part A* 106 (6) (2018) 1535–1542, <https://doi.org/10.1002/jbma.a.36349>.
- [23] M. Abazari, T. Akbari, M. Hasani, E. Sharifkoulouei, M. Raoufi, A. Foroumadi, M. Sharifzadeh, L. Firoozpour, M. Khoobi, Polysaccharide-based hydrogels containing herbal extracts for wound healing applications, *Carbohydr. Polym.* 294 (2022) 119808, <https://doi.org/10.1002/j.carbpol.2022.119808>.
- [24] N. Raina, R. Pahwa, V.K. Thakur, M. Gupta, Polysaccharide-based hydrogels: new insights and futuristic prospects in wound healing, *Int. J. Biol. Macromol.* 223 (2022) 1586–1603, <https://doi.org/10.1016/j.ijbiomac.2022.11.115>.
- [25] X. Wang, R. Song, M. Johnson, S. A., P. Shen, N. Zhang, I. Lara-Sáez, Q. Xu, W. Wang, Chitosan-based hydrogels for infected wound treatment, *Macromol. Biosci.* 23 (9) (2023) 2300094, <https://doi.org/10.1002/mabi.202300094>.
- [26] S. Torkaman, H. Rahmani, A. Ashori, S.H.M. Najafi, Modification of chitosan using amino acids for wound healing purposes: a review, *Carbohydr. Polym.* 258 (2021) 117675, <https://doi.org/10.1016/j.carbpol.2021.117675>.
- [27] A. Noori, M. Hoseinpour, S. Kolivand, N. Lotfibakhshaeish, M. Azami, J. Ai, S. Ebrahimi-Barough, Synergy effects of copper and L-arginine on osteogenic, angiogenic, and antibacterial activities, *Tissue Cell* 77 (2022) 101849, <https://doi.org/10.1016/j.tice.2022.101849>.
- [28] Z. Ling, J. Deng, Z. Zhang, H. Sui, W. Shi, B. Yuan, H. Lin, X. Yang, J. Cao, X. Zhu, X. Zhang, Spatiotemporal manipulation of L-arginine release from bioactive hydrogels initiates rapid skin wound healing accompanied with repressed scar formation, *Appl. Mater. Today* 24 (2021) 101116, <https://doi.org/10.1016/j.apmt.2021.101116>.
- [29] H.C. Bygd, D. Akilbekova, A. Muñoz, K.D. Forsmark, K.M. Bratlie, Poly-L-arginine based materials as instructive substrates for fibroblast synthesis of collagen, *Biomaterials* 63 (2015) 47–57, <https://doi.org/10.1016/j.biomaterials.2015.05.045>.
- [30] H. Ma, Y. He, L. Xu, Y. Wei, Fabrication of polydopamine/hemin-cyclodextrin supramolecular assemblies for mimicking natural peroxidases and their sensitive detection of cholesterol, *J. Mol. Liq.* 328 (2021) 115490, <https://doi.org/10.1016/j.molliq.2021.115490>.
- [31] J. Ma, P. Yu, B. Xia, Y. An, Z. Wang, Synthesis of a biodegradable and environmentally friendly shale inhibitor based on chitosan-grafted L-arginine for wellbore stability and the mechanism study, *ACS Appl. Bio Mater.* 2 (10) (2019) 4303–4315, <https://doi.org/10.1021/acsabm.9b00566>.
- [32] X. Zhao, P. Li, B. Guo, P.X. Ma, Antibacterial and conductive injectable hydrogels based on quaternized chitosan-graft-polyaniline/oxidized dextran for tissue engineering, *Acta Biomater.* 26 (2015) 236–248, <https://doi.org/10.1016/j.actbio.2015.08.006>.
- [33] G. Gao, Y.-W. Jiang, H.-R. Jia, F.-G. Wu, Near-infrared light-controllable on-demand antibiotics release using thermo-sensitive hydrogel-based drug reservoir for combating bacterial infection, *Biomaterials* 188 (2019) 83–95, <https://doi.org/10.1016/j.biomaterials.2018.09.045>.
- [34] Q. Xu, M. Chang, Y. Zhang, E. Wang, M. Xing, L. Gao, Z. Huan, F. Guo, J. Chang, PDA/cn bioactive hydrogel with “hot ions effect” for inhibition of drug-resistant Bacteria and enhancement of infectious skin wound healing, *Appl. Mater. Interfaces.* 12 (28) (2020) 31255–31269, <https://doi.org/10.1021/acsami.0c08890>.
- [35] Y. Zhou, Q. Du, Q. Zhao, M. Zhang, X. Qin, Y. Jiang, Y. Luan, A heme-regulatable chemodynamic nanodrug harnessing transcription factor Bach1 against lung cancer metastasis, *J. Colloid Interf. Sci.* 610 (2022) 698–708, <https://doi.org/10.1016/j.jcis.2021.11.124>.
- [36] M. Zhang, Z. Fan, J. Zhang, Y. Yang, C. Huang, W. Zhang, D. Ding, G. Liu, N. Cheng, Multifunctional chitosan/alginate hydrogel incorporated with bioactive glass nanocomposites enabling photothermal and nitric oxide release activities for bacteria-infected wound healing, *Int. J. Biol. Macromol.* 232 (2023) 123445, <https://doi.org/10.1016/j.ijbiomac.2023.123445>.
- [37] K. Zhou, Z. Zhang, J. Xue, J. Shang, D. Ding, W. Zhang, Z. Liu, F. Yan, N. Cheng, Hybrid ag nanoparticles/polyoxometalate-polydopamine nano-flowers loaded chitosan/gelatin hydrogel scaffolds with synergistic photothermal/chemodynamic/ag+ anti-bacterial action for accelerated wound healing, *Int. J. Biol. Macromol.* 221 (2022) 135–148, doi:10.1016/j.ijbiomac.2022.08.151.
- [38] B.P. Antunes, A.F. Moreira, V.M. Gaspar, I.J. Correia, Chitosan/arginine-chitosan polymer blends for assembly of nanofibrous membranes for wound regeneration, *Carbohydr. Polym.* 130 (2015) 104–112, <https://doi.org/10.1016/j.carbpol.2015.04.072>.
- [39] Y. Chen, S. Zhou, Q. Li, Microstructure design of biodegradable scaffold and its effect on tissue regeneration, *Biomaterials* 32 (22) (2011) 5003–5014, <https://doi.org/10.1016/j.biomaterials.2011.03.064>.
- [40] R. Augustine, N. Kalairikkal, S. Thomas, An in vitro method for the determination of microbial barrier property (MBP) of porous polymeric membranes for skin substitute and wound dressing applications, *Tissue Eng. Regen. Med.* 12 (1) (2015) 12–19, <https://doi.org/10.1007/s13770-014-0032-9>.
- [41] Y. Zhang, K. Zhang, H. Yang, Y. Hao, J. Zhang, W. Zhao, S. Zhang, S. Ma, C. Mao, Highly penetrable drug-loaded Nanomotors for Photothermal-enhanced Ferroptosis treatment of tumor, *Appl. Mater. Interfaces* 15 (11) (2023) 14099–14110, <https://doi.org/10.1021/acsmi.3c00297>.
- [42] A. Ali, J. Liu, H. Zhou, T. Liu, M. Ovais, H. Liu, Y. Rui, C. Chen, Graphdiyne–hemin-mediated catalytic system for wound disinfection and accelerated wound healing, *Mater. Chem. Front.* 5 (16) (2021) 6041–6051, <https://doi.org/10.1039/D1QM00490E>.
- [43] C. Zhao, X. Wu, G. Chen, F. Wang, J. Ren, AuNPs-PCL nanocomposite accelerated abdominal wound healing through photothermal effect and improving cell adhesion, *J. Biomater. Sci. Polym. Ed.* 29 (16) (2018) 2035–2049, <https://doi.org/10.1080/09205063.2018.1526460>.
- [44] A. Capon, E. Souil, B. Gauthier, C. Sumian, M. Bachelet, B. Buys, B.S. Polla, S. Mordon, Laser assisted skin closure (LASC) by using a 815-nm diode-laser system accelerates and improves wound healing, *Lasers Surg. Med.* 28 (2) (2001) 168–175, <https://doi.org/10.1002/lsm.1035>.
- [45] J. He, Z. Li, J. Wang, T. Li, J. Chen, X. Duan, B. Guo, Photothermal antibacterial antioxidant conductive self-healing hydrogel with nitric oxide release accelerates diabetic wound healing, *Compos. B. Eng.* 266 (2023) 110985, <https://doi.org/10.1016/j.compositesb.2023.110985>.
- [46] K. Zhou, Z. Zhang, J. Xue, J. Shang, D. Ding, W. Zhang, Z. Liu, F. Yan, N. Cheng, Hybrid ag nanoparticles/polyoxometalate-polydopamine nano-flowers loaded chitosan/gelatin hydrogel scaffolds with synergistic photothermal/chemodynamic/ag+ anti-bacterial action for accelerated wound healing, *Int. J. Biol. Macromol.* 221 (2022) 135–148, <https://doi.org/10.1016/j.ijbiomac.2022.08.151>.
- [47] B. Tao, C. Lin, Y. Deng, Z. Yuan, X. Shen, M. Chen, Y. He, Z. Peng, Y. Hu, K. Cai, Copper-nanoparticle-embedded hydrogel for killing bacteria and promoting wound healing with photothermal therapy, *J. Mater. Chem. B* 7 (15) (2019) 2534–2548, <https://doi.org/10.1039/C8TB03272F>.
- [48] X. He, L. Dai, L. Ye, X. Sun, O. Enoch, R. Hu, X. Zan, F. Lin, J. Shen, A vehicle-free antimicrobial polymer hybrid gold nanoparticle as synergistically therapeutic platforms for *Staphylococcus aureus* infected wound healing, *Adv. Sci.* 9 (14) (2022) 2105223, <https://doi.org/10.1002/advs.202105223>.
- [49] Y. Liang, M. Wang, Z. Zhang, G. Ren, Y. Liu, S. Wu, J. Shen, Facile synthesis of ZnO QDs@GO-CS hydrogel for synergistic antibacterial applications and enhanced wound healing, *Chem. Eng. J.* 378 (2019) 122043, <https://doi.org/10.1016/j.cej.2019.122043>.

Update

International Journal of Biological Macromolecules

Volume 302, Issue , April 2025, Page

DOI: <https://doi.org/10.1016/j.ijbiomac.2025.139996>



Corrigendum

Corrigendum to “Multifunctional polydopamine/hemin-cyclodextrin reinforced chitosan nanocomposite hydrogel: A synergistic platform for wound healing” [Int. J. Biol. Macromol. 260 (2024) 129553]



Xu-Mei Zhang ^a, Man Zhang ^{b,c}, Ning-Ning Xu ^d, Shu-Juan Zheng ^{d,*,**}, Ni Cheng ^c

^a Department of Pathology, Affiliated Hospital of Weifang Medical University, Weifang, Shandong 261053, PR China

^b Department of Pharmacy, The First People's Hospital of Aksu Prefecture, Aksu, Xinjiang 843000, PR China

^c College of Pharmacy, Weifang Medical University, Weifang, Shandong 261053, PR China

^d Department of General Surgery, Affiliated Hospital of Weifang Medical University, Weifang, Shandong 261053, PR China

The authors regret that due to an error during the manuscript preparation process, incorrect images were inadvertently included in

no change in the body text of the article.

Corrigendum Fig. 5: The corrected figure is shown as below.

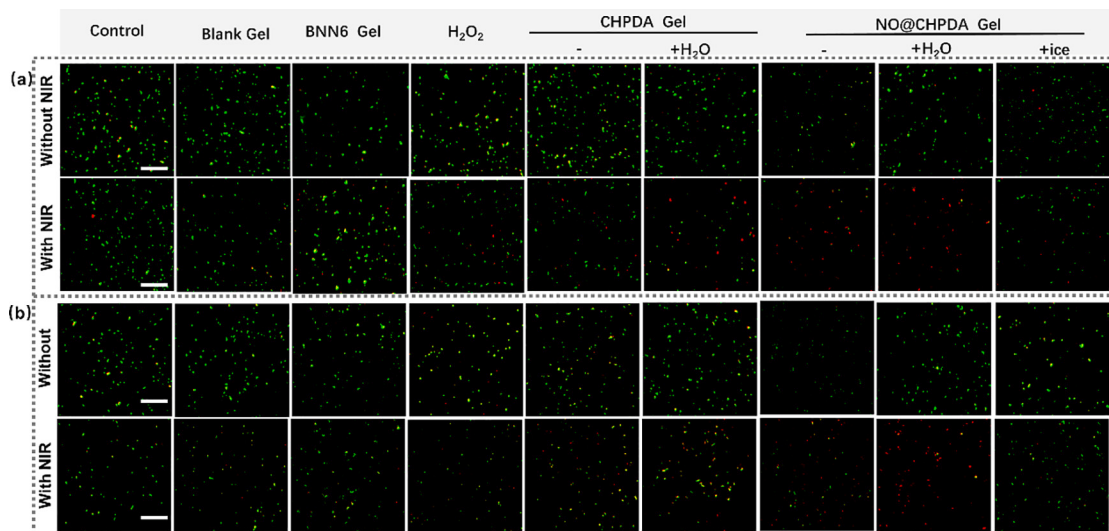


Fig. 5. Fluorescence images capturing *S. aureus* (a) and *E. coli* (b) bacteria subjected to various treatments with DMAO and EthD-III double staining.

Fig. 5. The correct and final version follows. All listed authors have approved the corrigendum. The authors would like to assert that there is

The authors would like to apologise for any inconvenience caused.

DOI of original article: <https://doi.org/10.1016/j.ijbiomac.2024.129553>.

* Corresponding author at: Department of General Surgery, Affiliated Hospital of Weifang Medical University, 518# Fuyuan Street, Weifang 261053, Shandong, PR China.

** Corresponding author at: College of Pharmacy, Weifang Medical University, 7166# Baotong West Street, Weifang 261053, Shandong, PR China.

E-mail addresses: 1518391145@qq.com, chengnmcn@163.com (S.-J. Zheng).